Sequential ARAIM Evaluation Using Time-Domain Versus Frequency-Domain Error-Correlation Bounding Methods

Danielle Racelis, Sandeep Jada, Mathieu Joerger
Virginia Tech, Blacksburg, VA

Danielle Racelis obtained a bachelor's degree (2014) in mechanical engineering from University of the Philippines, and a bachelor's (2017) and master's degree (2019) in aerospace engineering from University of Arizona. She is a PhD student at Virginia Tech, working with Dr. Mathieu Joerger, on navigation integrity using multi-constellation GNSS and LEO satellite constellations, in the Navigation laboratory for Autonomous Vehicle inTegrity (NAViTi).

Sandeep Jada obtained a master's degree (2011) in aerospace engineering from Indian Institute of Science, Bangalore, India. He worked for Airbus India (2011 to 2018). He is a doctoral candidate at Virginia Tech working with Dr. Mathieu Joerger, with a focus on error time correlation modeling and GNSS interference detection.

Dr. Mathieu Joerger (M.S., INSA Strasbourg - Illinois Tech, 2002; Ph.D., Illinois Tech 2009) is assistant professor at Virginia Tech, senior editor of Navigation for IEEE TAES, member of EU/US Cooperation on Satellite Navigation, Working Group C - ARAIM.

Abstract

In this paper, we evaluate the performance of a carrier-phase-based sequential implementation of Advanced Receiver Autonomous Integrity Monitoring (ARAIM). In particular, we analyze the robust modeling of measurement error dynamics over time, which is a major challenge in the design and evaluation of high-integrity sequential estimators and detectors. Two classes of methods were recently developed to rigorously account for time-correlated measurement errors: time-domain bounding [1, 2, 3, 4], and frequency-domain bounding [5, 6, 7]. We implement two of these methods [4, 7], analyze their differences with an illustrative example, and evaluate their integrity and continuity performance for an example ARAIM application.

1. Introduction

This work focuses on safety critical navigation applications where integrity is of primary concern. Integrity is a measure of trust in sensor information, and integrity risk is the probability of a system providing errors that are out of tolerance without timely warning. Advanced Receiver Autonomous Integrity Monitoring (ARAIM) is under development for Global Navigation Satellite Systems (GNSS)-based aircraft navigation. ARAIM is a self-contained method to check measurement consistency, which is used to protect the user from rarely occurring satellite and constellation faults. The European Union and the U.S. have joint initiatives through Working Group C, that aim at evaluating the potential of multi-constellation GNSS to achieve worldwide en route positioning (Horizontal ARAIM, or H-ARAIM) and vertical guidance of aircraft (Vertical ARAIM, or V-ARAIM) [8, 9, 10].

The baseline snapshot V-ARAIM algorithm, which uses carrier-smoothed code measurements at one instant in time, achieves high availability under nominal conditions. However, cases were found where this is not true, for example during satellite outages, i.e., under depleted GPS and/or Galileo constellations [9]. Sequential ARAIM can potentially mitigate this availability risk by processing measurements over time at the cost of a slightly higher computational load [11]. However, for sequential ARAIM to be a valid alternative, measurement error time-correlation models must be derived. While *snapshot* error models for GPS and Galileo are established using overbounding theory and many years of GPS and Galileo data analysis [12, 13], error dynamics *over time* has not been as thoroughly evaluated, until recently.

Langel et al. [1, 5] propose new error modeling methods that could rigorously account for uncertain time correlation in measurement errors, and for its impact on estimation errors. The proposed methods were analytically proven to be bounding. Years of GPS and Galileo data were processed [3, 6] to derive measurement error models. However, it remains unclear under which circumstances estimation error bounds are tighter using frequency-domain versus time-domain methods.

In response, for fair comparison between the two approaches, we implement the error bounding procedures in [4, 7]. We incorporate the resulting error time-correlation models into a sequential implementation of ARAIM, and perform a worldwide availability and coverage analysis using GPS and Galileo.

34th International Technical Meeting of the Satellite Division of the Institute of Navigation (ION GNSS+ 2021), September 20-24, 2021

1079

https://doi.org/10.33012/2021.18037

The error bounding procedures in [4] and [7] are not the focus of this paper. Rather, we provide but a short description of the two methods in Section 2. We then focus on comparing the estimation error bounds using the theorems in [1, 5]. Performance is evaluated using an illustrative example estimator in Section 3, and then using a worldwide integrity and continuity analysis in Section 4. For operations over the same fixed interval, we determine which of the time-domain versus frequency-domain error bounding methods provides a tighter integrity risk bound.

2. Error Bounding Methods

In high integrity applications, we must upper bound the probability of the estimation error exceeding predefined limits without an alert. Therefore, to be safe, we want to design measurement error models that produce state estimation error variances guaranteed to bound the true state estimation error variances. Several bounding schemes have been developed in recent years [1, 2, 14, 3, 4, 5, 6, 15, 16, 17, 18, 19, 20, 21, 7]. These can be broadly classified into two classes: time-domain bounding, and frequency-domain bounding. In both classes, a two-parameter (variance and time constant) first order Gauss Markov process (FOGMP) can be used as measurement error time-correlation bounding function because it is easily incorporated in linear estimators.

2.1. Time-Domain Error Bounding Method

Real measurement errors rarely behave like an FOGMP [3, 22, 23]. To address this issue, Langel, et al. developed a method that uses a pair of FOGMP autocorrelation functions (ACFs) to lower and upper bound the unknown, non-FOGMP error ACF [1].

In order to derive bounding FOGMP model in the time domain, we leverage the method developed in [4]. Instead of bounding measurement error ACFs, we bound the distribution of measurement error lagged products over all lag times. The lagged products distribution quantile bounding process is described in [4].

2.2. Frequency-Domain Error Bounding Method

The Wiener-Khintchine theorem states that the power spectral density (PSD) and the ACF are a Fourier transform pair [24]. The frequency-domain method uses this theorem, and uses sample PSD upper-bounding to model measurement error time-correlation. Based on [17, 20], a time-correlation model whose PSD upper-bounds the measurement error PSD, guarantees an upper bound on the state estimation error variance. The methods proposed in [17] and [20] estimate measurement error PSDs from data, and upper bound these PSD estimates with a FOGMP PSD. With this approach, the upper bounding PSD is determined by the worst measurement error PSD estimate, which can lead to conservative time-correlation models [7].

The PSD bounding method in [17, 20] is refined in [7], where instead of bounding measurement error PSD estimates, it bounds quantiles of the distribution of measurement error scaled periodograms. This approach leverages the fact that the mean of the scaled periodogram distribution is the PSD, and an upper bound on the scaled periodogram distribution is guaranteed to upper bound the PSD [7]. We use the process in [7] for frequency-domain error-bounding.

2.3. Error Bounding Example Using Simulated Data

We simulated measurement errors using 2000 sample paths (i.e., sample fixed-interval measurement sequences), each 100 seconds in length, generated from a FOGMP with unit variance and time constant of 50 seconds. We use this example data set to illustrate the bounding methods in a controlled scenario, where the only source of uncertainty stems from the limited number of data samples. If errors were actually FOGMP processes, and if we had an infinite number data samples, the time-domain and frequency-domain models would converge. Actual data are impacted by other sources of uncertainty including the fact that empirical stochastic processes are not FOGMPs and are not startionary over long time periods [3, 6].

Note that ACF and PSD estimation is more of an art, and is inexact for finite data. There is often a tradeoff between model fidelity to data, and noisiness of the estimate [7]. To reduce the uncertainty associated with ACF and PSD estimation, we use the streamlined time-domain bounding process in [4] and frequency-domain bounding process in [7].

The time-correlation models for time-domain and frequency-domain methods are respectively shown in Figures 1 and 2. In Fig. 1, the upper and lower bounding FOGMP models are displayed on the top and bottom plots, respectively. The figures show measurement error lagged products in gray: for each sample path, the sample lagged products $(v_0 v_\tau)$ are the measurement error at time 0 (v_0) multiplied by the measurement error at a later time-epoch (v_{tau}), for τ ranging from 0 to the length of the sample path. The solid black lines represent quantiles of the lagged product distribution at lag times τ. For example, the topmost solid black line on the top plot of Fig. 1 represents the 95% percentile of the sample lagged products at tau values ranging from 0 to 100 seconds. The dashed

black lines represent theoretical quantiles of the model's FOGMP lagged product distribution. The FOGMP model was chosen such that all its quantile curves (including the ones displayed: 5%, 32%, 68%, 95%) upper bound the sample quantiles (solid black lines) for all τ. A similar approach is used to lower-bound the FOGMP model [4].
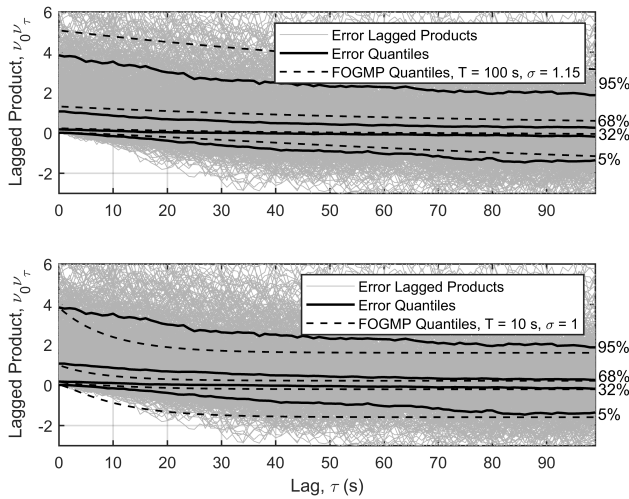

Figure 1: Time-domain bounding produces upper and lower bounding FOGMP lagged products distribution that upper and lower bound the measurement error lagged products distribution at four quantiles.
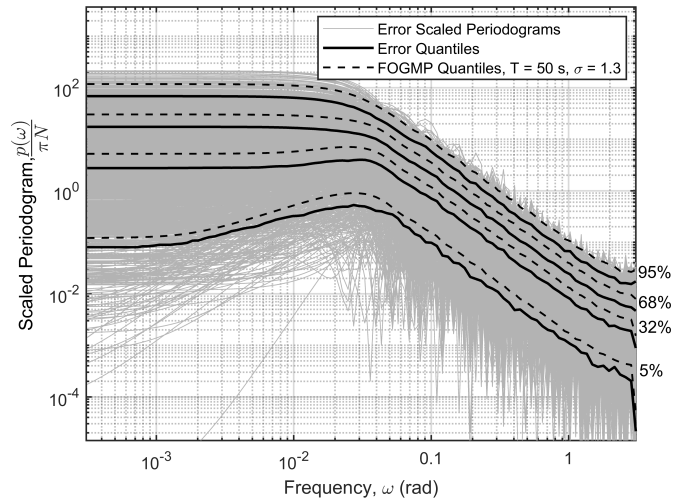

Figure 2: Frequency-domain bounding produces a FOGMP scaled periodogram distribution that upper bounds the measurement error scaled periodogram distribution at four quantiles.

The frequency-domain model derivation is illustrated in Fig. 2. Scaled periodograms for each sample path are shown in gray. The solid black lines represent sample quantiles of the error data scaled periodogram distribution over the frequency range of interest (the x-axis is expressed in terms of circular frequency [7]). The dashed black lines indicate quantiles of the upper bounding FOGMP model's scaled periodogram distribution over all frequencies. The plot shows that at the example quantiles, the FOGMP scaled periodogram distribution upper bounds the sample measurement error scaled periodogram distribution.

In time domain, the upper bounding FOGMP is described by its time constant $T_{max} = 100$ s, and standard deviation $\sigma_{max} = 1.15$, while the lower bounding FOGMP is described by $T_{min} = 100$ s, and $\sigma_{min} = 1$. For frequency domain, the upper bounding FOGMP model is described by $T_{freq} = 50$ s, and $\sigma_{freq} = 1.3$. Throughout our analysis, we observed that these six parameters typically satisfy the following inequalities

$$\sigma_{min} \leq \sigma_{max} \leq \sigma_{freq} \tag{1}$$

$$T_{min} \leq T_{freq} \leq T_{max} \ . \tag{2}$$

We use these model parameters in an example estimator in the next section.

3. Error Models Implemented in a Batch Least Squares Estimator

Given the discussion in Section 2, it is not clear which of the two methods will perform better. On one hand, time-domain bounding is tailored to the estimated state of interest, and uses two more parameters, i.e., σ_{min}^2, T_{min}, σ_{max}^2, T_{max}, to model the dynamics of the measurement error time-correlation. On the other hand, frequency-domain bounding is independent of the estimator. In addition, time-domain bounding is restricted to fixed-interval implementations due to the cumulative sizes of matrices that need to be stored, while frequency-domain bounding is compatible with recursive estimators such as Kalman filters. To be fair, we compare these two bounding methods when used for over a same fixed interval. In a fixed-interval implementation, neither method needs to assume a structure for the error time-correlation. They will be compared firstly, in the context of a simple least squares estimation example, and later in the context of a batch implementation of ARAIM.

Consider the following scalar least squares estimation example, where measurements at time 0 and a later time τ are used to estimate

the state x. The batch measurement equation is given by

$$\begin{bmatrix} z_0 \\ z_\tau \end{bmatrix} = \begin{bmatrix} h_0 \\ h_\tau \end{bmatrix} x + \begin{bmatrix} v_0 \\ v_\tau \end{bmatrix} \qquad \rightarrow \qquad \mathbf{z} = \mathbf{h}x + \mathbf{v} \tag{3}$$

where the measurement errors are zero-mean with unknown distribution $v \sim (0, \sigma_v)$. The objective of this section is to derive an expression for the state estimation error that would allow a proper comparison between the two error bounding methods. The least squares solution for the measurement vector in Eq. (3) is $\hat{x} = \left(\mathbf{h}^\mathrm{T}\mathbf{h}\right)^{-1}\mathbf{h}^\mathrm{T}\mathbf{z}$. The state estimation error is given by

$$\epsilon_{\hat{x}} = \hat{x} - x = \left(\mathbf{h}^\mathrm{T}\mathbf{h}\right)^{-1}\mathbf{h}^\mathrm{T}\left(\mathbf{h}x + \mathbf{v}\right) - x = \left(\mathbf{h}^\mathrm{T}\mathbf{h}\right)^{-1}\mathbf{h}^\mathrm{T}\mathbf{v} \tag{4}$$

$$= \underbrace{\frac{h_0}{h_0^2 + h_\tau^2}}\, v_0 + \underbrace{\frac{h_\tau}{h_0^2 + h_\tau^2}}\, v_\tau \tag{5}$$

$$= \quad s_0 \quad v_0 + \quad s_\tau \quad v_\tau \tag{6}$$

$$= \mathbf{s}^\mathrm{T}\mathbf{v} \tag{7}$$

where $\mathbf{s} = \begin{bmatrix} s_0 & s_\tau \end{bmatrix}^\mathrm{T}$ is a vector of estimator coefficients, whose dot product with the measurement vector returns the error in the state of interest x. We define an estimator matrix $\mathbf{M}$, and compute for the measurement error covariance matrix $\mathbf{V}$ to arrive at

$$\mathbf{M} = \mathbf{s}\mathbf{s}^\mathrm{T} = \begin{bmatrix} s_0^2 & s_0 s_\tau \\ s_0 s_\tau & s_\tau^2 \end{bmatrix} \quad , \quad \mathbf{V} = \mathrm{E}\left[\mathbf{v}\mathbf{v}^\mathrm{T}\right] = \mathrm{E}\begin{bmatrix} v_0^2 & v_0 v_\tau \\ v_0 v_\tau & v_\tau^2 \end{bmatrix} = \begin{bmatrix} \sigma_v^2 & \mathrm{E}\left[v_0 v_\tau\right] \\ \mathrm{E}\left[v_0 v_\tau\right] & \sigma_v^2 \end{bmatrix}. \tag{8}$$

We can compute the state estimation error variance using $\sigma_\epsilon^2 = \mathrm{E}\left[\epsilon^2\right]$. Alternatively, we can use the matrices in Eq. (8) to express the state estimation error variance as

$$\sigma_{\hat{x}}^2 = \sum_{i=1}^{2}\sum_{j=1}^{2}(\mathbf{M} \circ \mathbf{V}) = \mathbf{M}_{1,1}\mathbf{V}_{1,1} + \mathbf{M}_{2,1}\mathbf{V}_{2,1} + \mathbf{M}_{1,2}\mathbf{V}_{1,2} + \mathbf{M}_{2,2}\mathbf{V}_{2,2} \tag{9}$$

where $\circ$ denotes element-wise matrix multiplication. Let the measurement errors be modeled as a zero-mean first-order Gauss-Markov process (FOGMP) with the following autocorrelation function (ACF)

$$r_v(\tau) = \mathrm{E}\left[v_0 v_\tau\right] = \sigma_v^2 e^{-\tau/T} \tag{10}$$

which is expressed as a function of the time difference between two measurements τ. T is the Markov process correlation time constant, and σ_v^2 is the Gauss-Markov process variance. The state estimation error assuming a FOGMP measurement error model therefore becomes

$$\sigma_{\hat{x}}^2 = \sum_{i=1}^{2}\sum_{j=1}^{2}\left(\begin{bmatrix} s_0^2 & s_0 s_\tau \\ s_0 s_\tau & s_\tau^2 \end{bmatrix} \circ \begin{bmatrix} \sigma_v^2 & \sigma_v^2 e^{-\tau/T} \\ \sigma_v^2 e^{-\tau/T} & \sigma_v^2 \end{bmatrix}\right) \tag{11}$$

where the element-wise products of $\mathbf{M}$ and $\mathbf{V}$ are combined depending on the sign of elements in $\mathbf{M}$. Note that the diagonal elements of $\mathbf{M}$ are always positive, while the off-diagonal elements can have either sign.

3.1. Example Implementation of Time-Domain Model

The state estimation error variance using the time-domain models is computed in the following manner. We first define the following matrices

$$\mathbf{V}_+ = \sigma_{max}^2 \begin{bmatrix} 1 & e^{-\tau/T_{max}} \\ e^{-\tau/T_{max}} & 1 \end{bmatrix} \quad , \quad \mathbf{M}_+ \quad \text{where} \quad \left[\mathbf{M}_+\right]_{i,j} = \begin{cases} \left[\mathbf{M}_+\right]_{i,j} & \text{if } \left[\mathbf{M}_+\right]_{i,j} \geq 0 \\ 0 & \text{otherwise} \end{cases} \tag{12}$$

$$\mathbf{V}_- = \sigma_{min}^2 \begin{bmatrix} 1 & e^{-\tau/T_{min}} \\ e^{-\tau/T_{min}} & 1 \end{bmatrix} \quad , \quad \mathbf{M}_- \quad \text{where} \quad \left[\mathbf{M}_-\right]_{i,j} = \begin{cases} \left[\mathbf{M}_-\right]_{i,j} & \text{if } \left[\mathbf{M}_-\right]_{i,j} < 0 \\ 0 & \text{otherwise} \end{cases} \tag{13}$$

and then solve for

$$\sigma_{\hat{x}}^2 = \sum_{i=1}^{2}\sum_{j=1}^{2}\left(\mathbf{M}_+ \circ \mathbf{V}_+ + \mathbf{M}_- \circ \mathbf{V}_-\right). \tag{14}$$

Equation (14) combines the measurement error contributions in the worst conspiring manner by using σ_{max}, T_{max} when the estimator coefficients are positive, and using σ_{min}, T_{min} when the estimator coefficients are negative. If the estimator coefficients are of the same sign, i.e., $s_0, s_\tau \geq 0$ or $s_0, s_\tau < 0$, Eq. (14) becomes

$$\sigma^2_{\hat{x},time,++} = \sum_{i=1}^{2}\sum_{j=1}^{2}\left(\begin{bmatrix} s_0^2 & s_0 s_\tau \\ s_0 s_\tau & s_\tau^2 \end{bmatrix} \circ \begin{bmatrix} \sigma^2_{max} & \sigma^2_{max}e^{-\tau/T_{max}} \\ \sigma^2_{max}e^{-\tau/T_{max}} & \sigma^2_{max} \end{bmatrix} + \begin{bmatrix} 0 & 0 \\ 0 & 0 \end{bmatrix} \circ \begin{bmatrix} \sigma^2_{min} & \sigma^2_{min}e^{-\tau/T_{min}} \\ \sigma^2_{min}e^{-\tau/T_{min}} & \sigma^2_{min} \end{bmatrix}\right) \tag{15}$$

$$= \sum_{i=1}^{2}\sum_{j=1}^{2}\left(\begin{bmatrix} s_0^2 & s_0 s_\tau \\ s_0 s_\tau & s_\tau^2 \end{bmatrix} \circ \begin{bmatrix} \sigma^2_{max} & \sigma^2_{max}e^{-\tau/T_{max}} \\ \sigma^2_{max}e^{-\tau/T_{max}} & \sigma^2_{max} \end{bmatrix}\right). \tag{16}$$

Otherwise, the estimator coefficients are of opposite signs, i.e., $s_0 \geq 0, s_\tau < 0$ or $s_0 < 0, s_\tau \geq 0$, and then

$$\sigma^2_{\hat{x},time,+-} = \sum_{i=1}^{2}\sum_{j=1}^{2}\left(\begin{bmatrix} s_0^2 & 0 \\ 0 & s_\tau^2 \end{bmatrix} \circ \begin{bmatrix} \sigma^2_{max} & \sigma^2_{max}e^{-\tau/T_{max}} \\ \sigma^2_{max}e^{-\tau/T_{max}} & \sigma^2_{max} \end{bmatrix} + \begin{bmatrix} 0 & s_0 s_\tau \\ s_0 s_\tau & 0 \end{bmatrix} \circ \begin{bmatrix} \sigma^2_{min} & \sigma^2_{min}e^{-\tau/T_{min}} \\ \sigma^2_{min}e^{-\tau/T_{min}} & \sigma^2_{min} \end{bmatrix}\right) \tag{17}$$

$$= \sum_{i=1}^{2}\sum_{j=1}^{2}\left(\begin{bmatrix} s_0^2 & s_0 s_\tau \\ s_0 s_\tau & s_\tau^2 \end{bmatrix} \circ \begin{bmatrix} \sigma^2_{max} & \sigma^2_{min}e^{-\tau/T_{min}} \\ \sigma^2_{min}e^{-\tau/T_{min}} & \sigma^2_{max} \end{bmatrix}\right). \tag{18}$$

3.2. Example Implementation of Frequency-Domain Model

The state estimation error variance using the frequency-domain-derived models is simply

$$\sigma^2_{\hat{x},freq} = \sum_{i=1}^{2}\sum_{j=1}^{2}\left(\begin{bmatrix} s_0^2 & s_0 s_\tau \\ s_0 s_\tau & s_\tau^2 \end{bmatrix} \circ \begin{bmatrix} \sigma^2_{freq} & \sigma^2_{freq}e^{-\tau/T_{freq}} \\ \sigma^2_{freq}e^{-\tau/T_{freq}} & \sigma^2_{freq} \end{bmatrix}\right). \tag{19}$$

3.3. Elliptical Representation of Each Method's Measurement Error Covariance Matrix

We leverage the fact that the left hand side matrices in Eq. (16)-(19) are consistent all throughout, and compare error models in the measurement domain using the measurement error covariance matrices. We plot an elliptical representation of each method's measurement error covariance, i.e., the right hand side matrix in Eq. (16), (18), and (19). These matrices are

$$\mathbf{V}_{time} = \begin{cases} \sigma^2_{max}\begin{bmatrix} 1 & e^{-\tau/T_{max}} \\ e^{-\tau/T_{max}} & 1 \end{bmatrix} & \text{if } \begin{matrix} s_0, s_\tau \geq 0 \text{ or} \\ s_0, s_\tau < 0 \end{matrix} \\ \begin{bmatrix} \sigma^2_{max} & \sigma^2_{min}e^{-\tau/T_{min}} \\ \sigma^2_{min}e^{-\tau/T_{min}} & \sigma^2_{max} \end{bmatrix} & \text{if } \begin{matrix} s_0 \geq 0, s_\tau < 0 \text{ or} \\ s_0 < 0, s_\tau \geq 0 \end{matrix} \end{cases} \tag{20}$$

$$\mathbf{V}_{freq} = \sigma^2_{freq}\begin{bmatrix} 1 & e^{-\tau/T_{freq}} \\ e^{-\tau/T_{freq}} & 1 \end{bmatrix}. \tag{21}$$

We plot the corresponding measurement covariance ellipses at lag times $\tau = 5, 30, 76.22, 120, 300$ seconds. Consider the plot on Fig. 3. The x-axis represents measurement z_0, and the y-axis represents measurement z_τ. A pair of estimator coefficients $[s_0, s_\tau]$ describes a line that passes through the origin, with slope s_τ/s_0 as shown on Fig. 3.
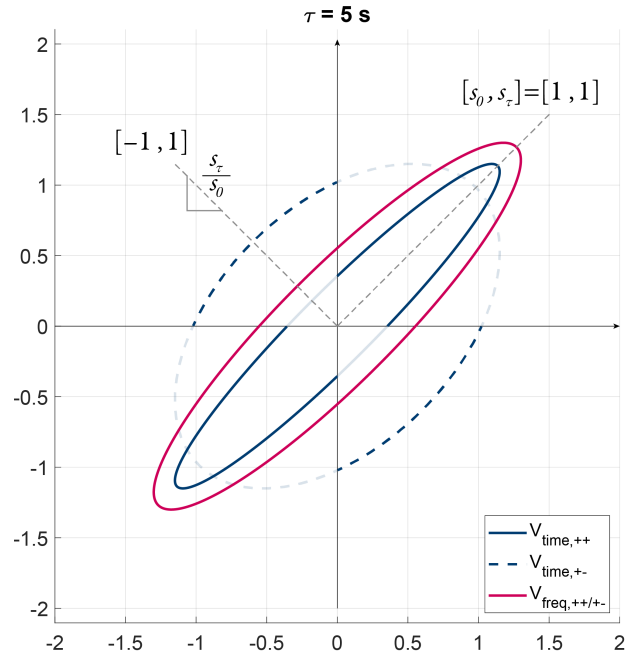

Figure 3: Measurement error covariance ellipse representation based on Eq. (20)-(21) for $\tau = 5$ s

Like-signed estimator coefficients combine measurements z_0 and z_τ in such a way that the state estimation error variance bound (solid blue ellipse) can lie in quadrants one and three only, while the state estimation error variance bound for oppositely-signed estimator coefficients (dashed blue ellipse) can lie in quadrants two and four. The frequency-domain ellipse is shown in magenta. Figures 3-4 show that at $\tau = 5$ s and $\tau = 30$ s, time-domain bound is tighter for like-signed estimator coefficients than the frequency-domain

bound. On the other hand, for oppositely signed estimator coefficients, the frequency-domain bound is tighter. At $\tau = 76.22$ s, on Fig. 4 where the dashed blue and magenta ellipses intersect, we see equal performance between the two methods for certain pairs of estimator coefficients lying along the $s_\tau/s_0 = -1$ line.
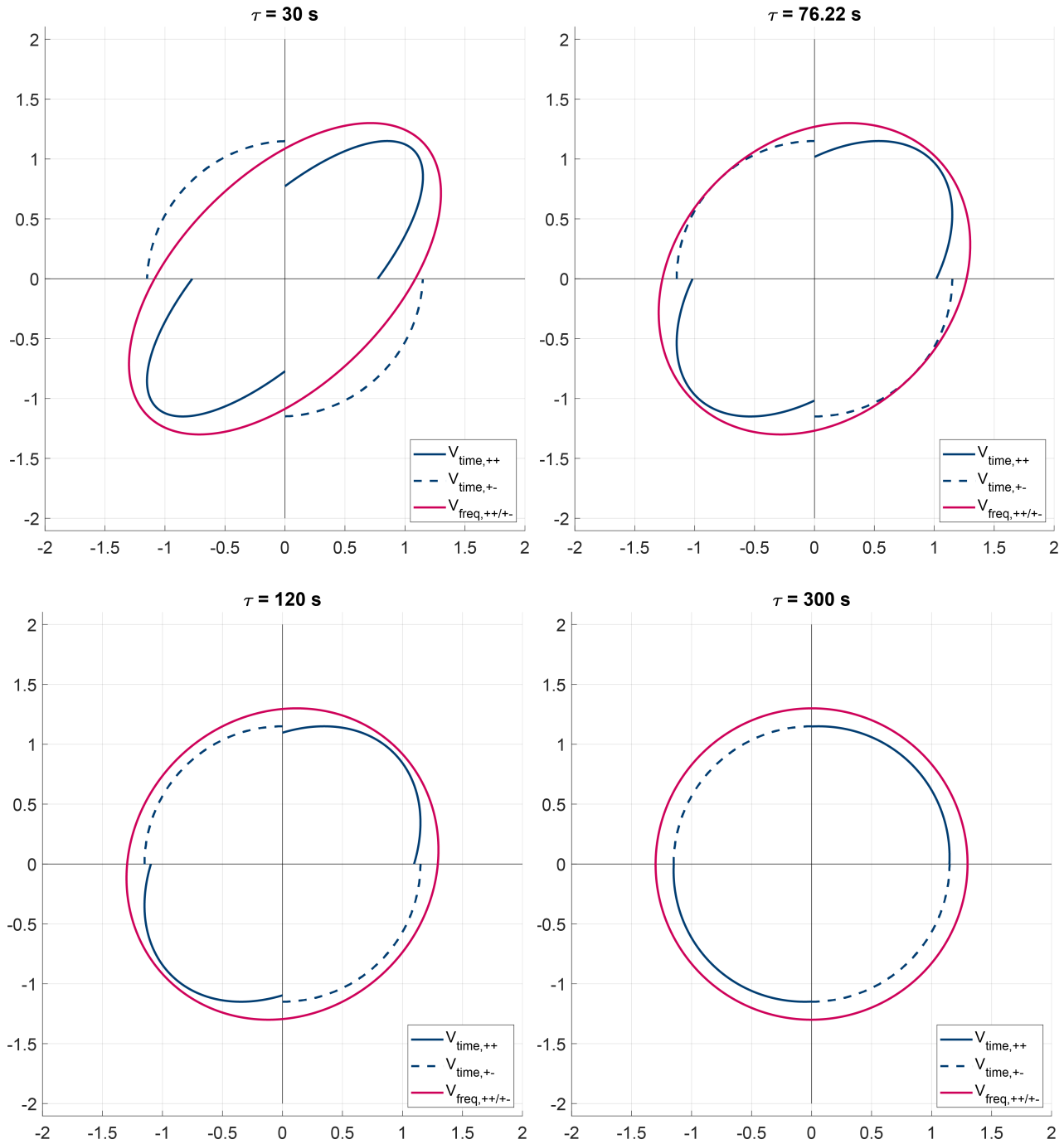

Figure 4: Measurement error covariance ellipse representation based on Eq. (20)-(21) for $\tau = 30$, 76.22, 120, and 300 s

Plotting the covariance ellipses at τ values greater than 76.22 s on Fig. 4 shows that the time-domain model is tighter. This exercise shows how either method could perform better when the time difference between measurements τ is less that the true error time constant $T = 50$ s. However, at τ values much larger than T, there is little time-correlation between measurements. Sources of error for which τ is more than twice T are typically treated as uncorrelated, even in high-integrity applications. Thus, the time-domain model performs better than the frequency-domain model for a limited range of sampling times that are longer than the measurement

error correlation time constant T, but not much longer than twice T. When $\tau < T$, the result is estimator dependent, but the larger T is relative to τ, the more conservative the time-domain approach becomes for estimator coefficients in the off-diagonal ($\pm$) quadrants. Thus, we may find tighter positioning error variance bounds for frequency domain versus time-domain if $\tau \ll T$. We consider a more realistic example using an ARAIM simulation.

4. VARAIM Application of Error Models

We now compare the time-domain and frequency-domain bounding methods in a carrier-phase-based implementation of Advanced Receiver Autonomous Integrity Monitoring (ARAIM). Ionosphere-free GPS and Galileo code and carrier measurements are filtered to simultaneously estimate three-dimensional position, receiver clock biases, and floating-valued cycle ambiguities. The integrity risk bound is calculated using a multiple hypothesis solution separation approach, where we use an optimal, risk-minimizing estimator [10], and account for the number of effectively independent samples when evaluating risk over time [25]. Our batch implementation of fault detection and exclusion closely follow the algorithm in [26], except that we compute integrity risk directly instead of protection levels [27].

4.1. Nominal Measurement Error Models Accounting for Time-Correlation

The linearized ionosphere-error-free carrier phase and code measurement equations for satellite i at time k respectively are

$$
\begin{aligned}
{}^i\phi_k &= -{}^i\mathbf{e}_k^{\mathrm{T}}\mathbf{x}_k + \tau_k + {}^i\eta + {}^i\mathscr{E}_{E,k} + {}^i\mathscr{E}_{T,k} + {}^i\mathscr{E}_{M,\phi,k} + {}^i\mathscr{E}_{R,\phi,k} \\
{}^i\rho_k &= -{}^i\mathbf{e}_k^{\mathrm{T}}\mathbf{x}_k + \tau_k \qquad\quad + {}^i\mathscr{E}_{E,k} + {}^i\mathscr{E}_{T,k} + {}^i\mathscr{E}_{M,\rho,k} + {}^i\mathscr{E}_{R,\rho,k}
\end{aligned}
\tag{22}
$$

where ${}^i\phi_k$ is the carrier phase measurement, ${}^i\rho_k$ is the code phase measurement, ${}^i\mathbf{e}_k$ is the 3×1 line-of-sight vector from the satellite to the user in North-East-Down (NED), $\mathbf{x}_k$ is the user position with respect to the linearization point, τ_k is the receiver clock offset (one for each constellation), ${}^i\eta$ is the carrier phase cycle ambiguity (there is no subscript k because it is constant over time), ${}^i\mathscr{E}_{E,k}$ is the satellite orbit and clock ephemeris error, ${}^i\mathscr{E}_{T,k}$ is the residual tropospheric error, ${}^i\mathscr{E}_{M,k}$ is the multipath error, and ${}^i\mathscr{E}_{R,k}$ is the receiver noise error. Each measurement error source was modelled in same way as in [27], and only briefly summarized here.

Satellite Orbit and Clock Ephemeris Error
The error due to satellite orbit and clock ephemeris for satellite i at time k is modelled as an FOGMP of the form ${}^i\mathscr{E}_{E,k} = e^{-T_s/T_E}\,{}^i\mathscr{E}_{E,k-1} + \nu_{E,k}$, with GMP variance σ_E^2, correlation time constant T_E, driving noise $\nu_{E,k}$, and sampling interval $T_s = t_k - t_{k-1}$. We assume no correlation between measurements from different satellites [28, 29, 30].

Residual Tropospheric Error
The bulk of the tropospheric delay error is removed using standard models of the troposphere [31]. We model the residual tropospheric error as an FOGMP scaled by an elevation-dependent mapping function [32]

$$
{}^i c_{T,k} = \frac{1.001}{\sqrt{0.002001 + (\sin({}^i\theta_k\,[\mathrm{rad}]))^2}}
\tag{23}
$$

for satellite elevation angles ${}^i\theta_k \geq 4°$. The resulting error contribution for satellite i at time k is given by ${}^i\mathscr{E}_{T,k} = {}^i c_{T,k}\,{}^i\zeta_{T,k}$ where the residual tropospheric error at zenith is modeled as ${}^i\zeta_{T,k} = e^{-T_s/T_T}\,{}^i\zeta_{T,k-1} + \nu_{T,k}$.

Multipath Error
Multipath error is modeled as an FOGMP, multiplied by an elevation-dependent mapping function

$$
{}^i c_{M,k} = c_{IF}\left(0.13 + 0.53\,e^{\left(-{}^i\theta_k\,[\mathrm{deg}]/10\right)}\right)
\tag{24}
$$

where $c_{IF} = \sqrt{\left(f_{L1}^4 + f_{L5}^4\right)\left(f_{L1}^2 - f_{L5}^2\right)^{-2}}$, and f_{L1} and f_{L5} are the frequencies for L1 and L5 respectively [31]. The multipath error contribution for satellite i at time k, for carrier and code measurements respectively are ${}^i\mathscr{E}_{M,\phi,k} = {}^i c_{M,k}\,{}^i\zeta_{M,\phi,k}$ and ${}^i\mathscr{E}_{M,\rho,k} = {}^i c_{M,k}\,{}^i\zeta_{M,\rho,k}$. The parameters are listed in Table 1, where the two orders of magnitude difference in multipath error between code and carrier is accounted for.

Receiver Noise Error
Receiver noise is modeled as Gaussian white noise such that the error contribution for carrier and code measurements respectively

are ${}^i\mathcal{E}_{R,\phi,k} \sim N(0, {}^i\sigma^2_{R,\phi})$, and ${}^i\mathcal{E}_{R,\rho,k} \sim N(0, {}^i\sigma^2_{R,\rho})$, where the elevation-dependent standard deviations are formulated as [32]

$$ {}^i\sigma_{R,\rho,k} = c_{IF}\left(0.11 + 0.13\,e^{\left(-{}^i\theta_k\,[\mathrm{deg}]/6.9\right)}\right) \tag{25}$$

$$ {}^i\sigma_{R,\phi,k} = \left(\frac{1}{100}\right) c_{IF}\left(0.11 + 0.13\,e^{\left(-{}^i\theta_k\,[\mathrm{deg}]/6.9\right)}\right)\,. \tag{26}$$

Measurement Error Parameters

To keep to the controlled manner of comparison between time-domain and frequency-domain bounding, where the only uncertainty is finiteness of data, we keep using simulated data. A Monte Carlo simulation is used to generate measurement error time histories for ephemeris orbit and clock, trophospheric delay, multipath, and receiver noise. The FOGMP parameters used to generate the true error time histories are given in Appendix A. The resulting FOGMP error model parameters for time and frequency-domain bounding are given in Table 1.

Table 1: Summary of Error Parameters

| Error Source	Mapping Function	Time-Domain				Frequency-Domain	
		σ_{min}	σ_{max}	T_{min}	T_{max}	σ_{freq}	T_{freq}
Ephemeris (GPS)		2.4 m	2.6 m	900 min	2500 min	2.7 m	1500 min
Ephemeris (Galileo)		6.0 m	6.2 m	700 min	2000 min	7.2 m	1070 min
Troposphere	Eq. (23)	0.12 m	0.13 m	20 min	50 min	0.14 m	25 min
Code Multipath	Eq. (24)	0.83 m	0.9 m	300 s	915 s	2.2 m	420 s
Carrier Multipath	Eq. (24)	0.0083 m	0.009 m	300 s	915 s	0.022 m	420 s
Receiver Code Noise				Eq. (25)			
Receiver Carrier Noise				Eq. (26)			
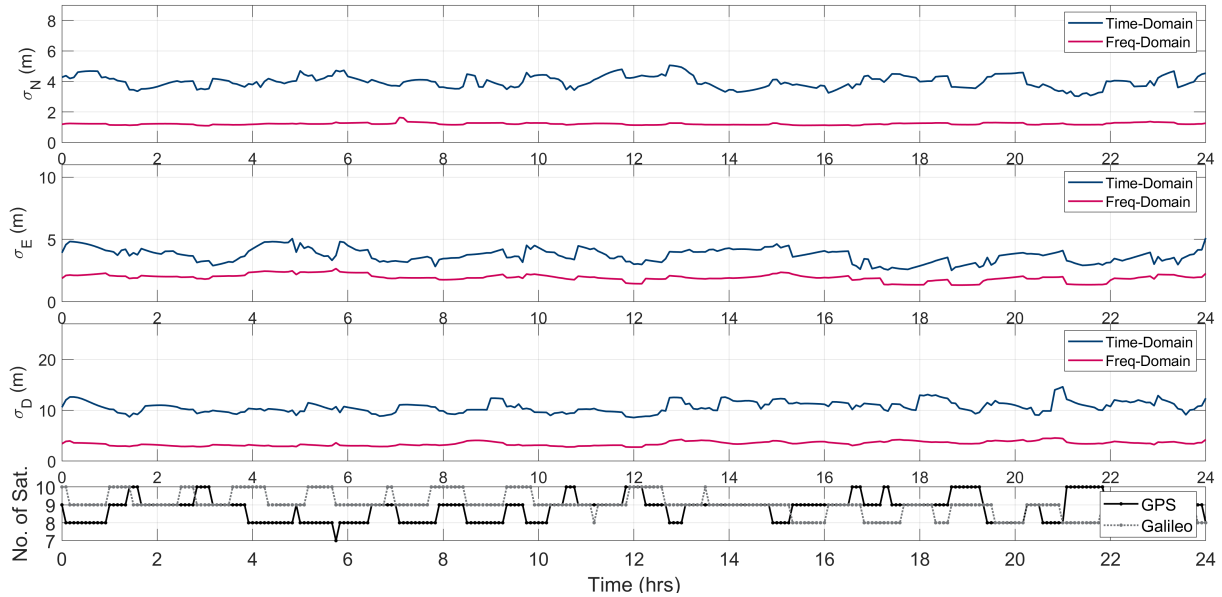
Figure 5: Comparison of time-domain and frequency-domain bounding for one location over 24 hours.

4.2. Batch Measurement Equation

A batch weighted least squares algorithm is used to simultaneously estimate the three-dimensional user position and receiver clock offsets at every time step, and the floating valued carrier phase cycle ambiguities that are constant over time, as long as the carrier is continuously tracked. For practical applications, this method can be implemented sequentially in a sliding window mechanism, as long as adequate receiver memory is available to store current and past measurements. Using a batch lets us forgo making an assumption on the structure of the actual measurement error time-correlation for the time-domain approach, and therefore enables a fair comparison between time-domain bounding and frequency-domain bounding. The batch measurement equation and measurement error covariance is derived in Appendix B.

4.3. Local Availability Analysis

The example uses a 10-minute batch. Within the batch, measurements are sampled every 5 minutes for the batch estimator. This 10-minute batch is evaluated repeatedly at regular 5-minute intervals over 24 hours at a reference location 0°N 0°W 0m altitude. Note that we are sampling measurements at 5 minutes, which is much less than the dominating error source time constant, i.e., the ephemeris error time constant. We plot the fault free user position standard deviation at current time, in North, East, Down, as well as the number of satellites in view for GPS and Galileo on Fig. 5. We see that the frequency-domain model in magenta, gives better performance than the time-domain model in blue.

Figure 6 compares the integrity risk (probability of hazardously misleading information, P_{HMI}) of time-domain and frequency-domain bounding for the same location over 24 hours. The parameters used for fault detection, exclusion, and integrity risk evaluation is given Appendix Appendix C. We see that frequency-domain bounding performs better than time-domain bounding for the entire simulation period, which is not unexpected based on the analysis in Section 3 because $T_E \gg T_S$.
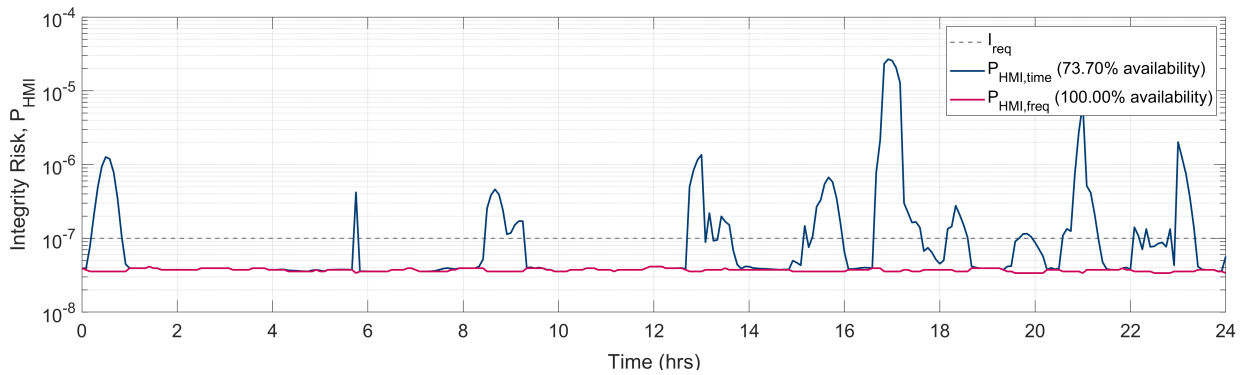

Figure 6: Comparison of time-domain and frequency-domain bounding for one location over 24 hours.

4.4. Global Availability Analysis

We extend our analysis to a worldwide grid of locations and evaluate integrity performance for all locations. A 10-minute batch is simulated at regular 30-minute intervals for 24 hours. Measurements are sampled for the estimator every five minutes. Reference locations were simulated on a $10° \times 10°$ latitude-longitude grid. Constellations in use were 24-satellite GPS and 24-satellite Galileo.
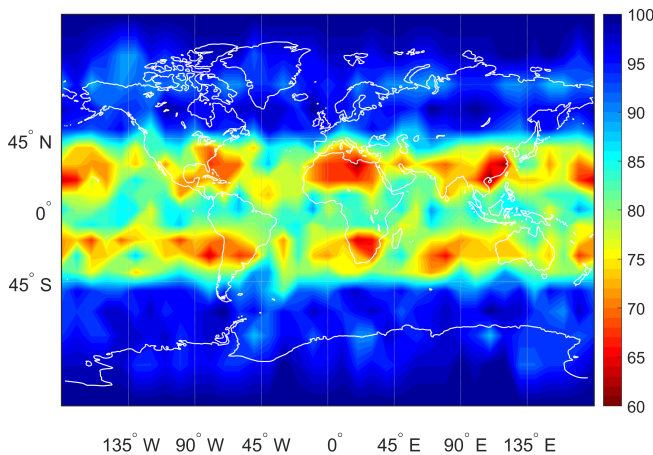

Figure 7: Time-domain bounding provides 50.52% coverage of 100% availability for example ARAIM simulation using Table 1 and Appendix C parameters.
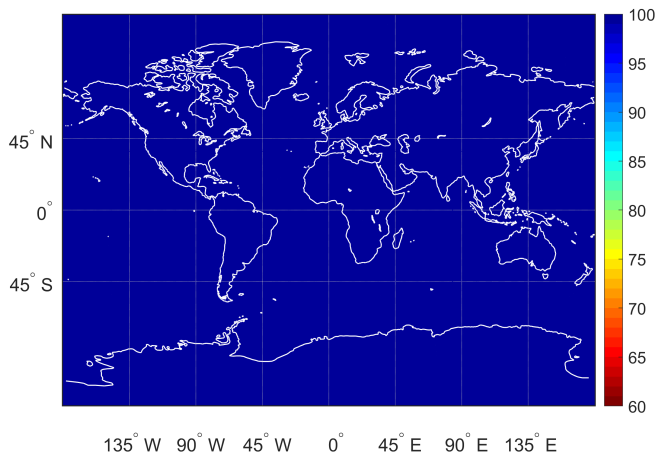
Figure 8: Frequency-domain bounding provides 100% coverage of 100% availability for example ARAIM simulation using Table 1 and Appendix C parameters.

The color bars on Fig. 7-8 indicate availability, which is the fraction of time over 24 hours, that the integrity risk bound is below the integrity risk requirement. The frequency-domain model provides better 100% availability coverage than the time-domain models. Although our example is ARAIM-based, the application of these error bounding methods can extend to many integrity-dependent applications that process measurements over time in sequential estimators.

5. Conclusions

In this paper, we analyzed the performance of time-domain versus frequency-domain bounding methods used to model time-correlated measurement errors in high-integrity sequential navigation applications. We first compared the tightness of the estimation error variance bounds in the context of a two-measurement scalar least squares estimation problem, where we used a measurement error covariance ellipse representation, to show that: (1) when the time difference τ between measurements is larger than the dominating error correlation time constant T but no more than twice T (i.e., $T < \tau < 2T$), then time-domain bounding can perform better, and (2) when the time difference between successive measurements is much less than the error correlation time constant ($\tau \ll T$), frequency-domain bounding can perform better.

We incorporated these new bounding methods into a sequential implementation of ARAIM, and performed a worldwide availability and coverage analysis using GPS and Galileo. We produced availability maps to capture the integrity and continuity performance of both methods. Based on this preliminary analysis, frequency-domain bounding can provide tighter integrity risk bounds than time-domain bounding. Thus, this paper provides a first look into the integrity performance of time-domain and frequency-domain bounding methods.

Appendix A. Monte Carlo Simulation of FOGMP Error Time Histories

The following table lists the FOGMP parameters used to generate the true measurement error time histories for ephemeris orbit and clock error, tropospheric error, and multipath error. A Monte Carlo simulation was implemented for each time-correlated error source by generating FOGMP's using σ and T.

Table 2: FOGMP Parameters Used in Monte Carlo Simulation of Measurement Error Time Histories

Error Source	σ	T
Ephemeris (GPS)	2.4 m	1620 min
Ephemeris (Galileo)	6.0 m	1200 min
Troposphere	0.12 m	30 min
Code Multipath	0.83 m	455 s
Carrier Multipath	0.0083 m	455 s

To generate the measurement error time history for each error source used in the ARAIM simulation, we start with an FOGMP time series $9000T$ long, where T is the last column on Table 2. For time-domain bounding we partition the $9000T$ long data into sample paths that are $3T$ long, giving us 3000 sample paths. We use sample paths $3T$ in length for time-domain modeling, because measurements made more than $3T$ apart can be considered uncorrelated [33]. For frequency-domain bounding, we partition the data into 1000 sample paths, each $9T$ long. For a fixed amount of data, longer sample path lengths ensures accuracy of the quantiles, but at the same time reduces model fidelity (a noisier estimate). On the other hand, using shorter path lengths to increase the number of sample paths, can produce smoother estimates, but can make the quantiles inaccurate [7]. We arrived at $9T$-long sample paths after tuning.

Appendix B. Batch Measurement Equation and Measurement Error Covariance

Starting with the linearized measurement equations for ionosphere-error-free carrier and code measurements Eq. (22), we can derive a batch measurement equation of the form $\mathbf{z} = \mathbf{H}\mathbf{x} + \mathbf{v}$ by first defining

$$\mathbf{u}_k = \begin{bmatrix} \mathbf{x}_k^{\mathrm{T}} & \tau_{GPS,k} & \tau_{Galileo,k} \end{bmatrix}^{\mathrm{T}}, \tag{27}$$

$${}^i\mathbf{g}_k^{\mathrm{T}} = \begin{bmatrix} -{}^i\mathbf{e}_k^{\mathrm{T}} & 1 & 0 \end{bmatrix} \text{ if satellite } i \text{ is a GPS satellite, and} \tag{28}$$

$${}^i\mathbf{g}_k^{\mathrm{T}} = \begin{bmatrix} -{}^i\mathbf{e}_k^{\mathrm{T}} & 0 & 1 \end{bmatrix} \text{ if satellite } i \text{ is a Galileo satellite.} \tag{29}$$

We stack the measurements over time for each satellite i for time instances 1 through K. The resulting geometry matrix, carrier and code measurements, carrier and code measurement noise vectors, and user states are respectively expressed as

$${}^i\mathbf{G} = \begin{bmatrix} {}^i\mathbf{g}_1^{\mathrm{T}} & & \mathbf{0} \\ & \ddots & \\ \mathbf{0} & & {}^i\mathbf{g}_K^{\mathrm{T}} \end{bmatrix} \quad {}^i\boldsymbol{\varphi} = \begin{bmatrix} {}^i\phi_1 \\ \vdots \\ {}^i\phi_K \end{bmatrix} \quad {}^i\boldsymbol{\rho} = \begin{bmatrix} {}^i\rho_1 \\ \vdots \\ {}^i\rho_K \end{bmatrix} \quad {}^i\mathbf{v}_\phi = \begin{bmatrix} {}^i\gamma_{\phi,1} \\ \vdots \\ {}^i\gamma_{\phi,K} \end{bmatrix} \quad {}^i\mathbf{v}_\rho = \begin{bmatrix} {}^i\gamma_{\rho,1} \\ \vdots \\ {}^i\gamma_{\rho,K} \end{bmatrix} \quad \mathbf{u} = \begin{bmatrix} \mathbf{u}_1 \\ \vdots \\ \mathbf{u}_K \end{bmatrix} \tag{30}$$

Measurements get stacked with carrier phase measurements first, followed by code measurements to get

$$
\begin{bmatrix} {}^1\boldsymbol{\varphi} \\ {}^2\boldsymbol{\varphi} \\ \vdots \\ {}^{n_{sat}}\boldsymbol{\varphi} \\ {}^1\boldsymbol{\rho} \\ {}^2\boldsymbol{\rho} \\ \vdots \\ {}^{n_{sat}}\boldsymbol{\rho} \end{bmatrix} = \begin{bmatrix} {}^1\mathbf{G} & \mathbf{1}_{K\times 1} & 0 & & 0 \\ {}^2\mathbf{G} & 0 & \mathbf{1}_{K\times 1} & & 0 \\ \vdots & \vdots & \vdots & \ddots & \vdots \\ {}^{n_{sat}}\mathbf{G} & 0 & 0 & & \mathbf{1}_{K\times 1} \\ {}^1\mathbf{G} & 0 & 0 & & 0 \\ {}^2\mathbf{G} & 0 & 0 & & 0 \\ \vdots & \vdots & \vdots & \ddots & \vdots \\ {}^{n_{sat}}\mathbf{G} & 0 & 0 & & 0 \end{bmatrix} \begin{bmatrix} \mathbf{u} \\ {}^1\eta \\ {}^2\eta \\ \vdots \\ {}^{n_{sat}}\eta \end{bmatrix} + \begin{bmatrix} {}^1\mathbf{v}_\phi \\ {}^2\mathbf{v}_\phi \\ \vdots \\ {}^{n_{sat}}\mathbf{v}_\phi \\ {}^1\mathbf{v}_\rho \\ {}^2\mathbf{v}_\rho \\ \vdots \\ {}^{n_{sat}}\mathbf{v}_\rho \end{bmatrix} \tag{31}
$$

where n_{sat} is the total number of visible satellites. The stack of measurements can be compactly written as

$$
\begin{bmatrix} \boldsymbol{\varphi} \\ \boldsymbol{\rho} \end{bmatrix} = \begin{bmatrix} \mathbf{G}_\phi & \mathbf{H}_N \\ \mathbf{G}_\rho & \mathbf{0} \end{bmatrix} \begin{bmatrix} \mathbf{u} \\ \boldsymbol{\eta} \end{bmatrix} + \begin{bmatrix} \mathbf{v}_\phi \\ \mathbf{v}_\rho \end{bmatrix} . \tag{32}
$$

The batch measurement error covariance matrix accounting for measurement error time correlation is given by

$$
\mathbf{V} = \begin{bmatrix} \mathbf{V}_E + \mathbf{V}_T & \mathbf{V}_E + \mathbf{V}_T \\ \mathbf{V}_E + \mathbf{V}_T & \mathbf{V}_E + \mathbf{V}_T \end{bmatrix} + \begin{bmatrix} \mathbf{V}_{\phi\phi,M} + \mathbf{V}_{\phi\phi,R} & \mathbf{0} \\ \mathbf{0} & \mathbf{V}_{\rho\rho,M} + \mathbf{V}_{\rho\rho,R} \end{bmatrix} \tag{33}
$$

where $\mathbf{V}_E$ is the ephemeris error covariance, $\mathbf{V}_T$ is the tropospheric error covariance, $\mathbf{V}_M$ is the multipath error covariance, and $\mathbf{V}_R$ is the receiver noise error covariance. The covariance matrix captures the fact that $\mathbf{V}_E$ and $\mathbf{V}_T$ are common to code and carrier measurements, while $\mathbf{V}_M$ and $\mathbf{V}_R$ are different for code and carrier measurements. For each satellite i these covariances are

$$
\begin{aligned} {}^i\mathbf{V}_E &= \sigma_E^2 \, \exp\left(-\frac{T_s}{T_E}\mathbf{B}\right), \\ {}^i\mathbf{V}_T &= \sigma_T^2 \, {}^i\mathbf{c}_T \, {}^i\mathbf{c}_T^T \circ \exp\left(-\frac{T_s}{T_T}\mathbf{B}\right), {}^i\mathbf{V}_R = \\ {}^i\mathbf{V}_M &= \sigma_M^2 \, {}^i\mathbf{c}_M \, {}^i\mathbf{c}_M^T \circ \exp\left(-\frac{T_s}{T_M}\mathbf{B}\right), \end{aligned} \begin{bmatrix} {}^i\sigma_{R,1}^2 & 0 & \dots & 0 \\ 0 & {}^i\sigma_{R,2}^2 & \ddots & \vdots \\ \vdots & \ddots & \ddots & 0 \\ 0 & \dots & 0 & {}^i\sigma_{R,K}^2 \end{bmatrix}, \text{ where } \mathbf{B} = \begin{bmatrix} 0 & 1 & 2 & \dots & K-1 \\ 1 & 0 & 1 & & \vdots \\ 2 & 1 & 0 & & \vdots \\ \vdots & & & \ddots & \\ K-1 & & & & 0 \end{bmatrix} . \tag{34}
$$

The matrix $\mathbf{B}$ is a Toeplitz matrix which arises from computing the cross-correlation terms between separate times whilst having a fixed sampling period. The symbol "$\circ$" indicates element-by-element multiplication of matrices, whereas "$\exp(\cdot)$" means element-wise exponential function applied to the matrix in parentheses. For error source ε, σ_ε^2 is the FOGMP variance, ${}^i\mathbf{c}_\varepsilon$ is the vector of elevation-dependent coefficients stacked at all times for satellite i, T_ε is the Markov process correlation time constant, and T_s is the sampling interval. A derivation of these time-correlated measurement error covariance matrices is described in the Appendix of [34].

Appendix C. Parameters for ARAIM Simulations

Table 3: Parameters for Detection, Exclusion, and Integrity Risk Evaluation

	Description	Value
I_{req}	total integrity budget	10^{-7}/approach [26]
C_{req}	continuity risk requirement to limit probability of false alarms	10^{-7}/approach [26]
P_{sat}	probability of single satellite fault (GPS, Galileo)	10^{-5}, 10^{-5} [10]
P_{const}	probability of constellation fault (GPS, Galileo)	10^{-8}, 10^{-4} [10, 35]
VAL	vertical alert limit	100 m
HAL	horizontal alert limit	100 m
$T_{EXP,int}$	exposure time for integrity	150 s [26]
$T_{EXP,cont}$	exposure time for continuity	150 s [26]
TTA	time-to-alert	150 s [26]
$MTTN$	mean-time-to-notify	1 h [10, 25, 26, 35]
$N_{ES,int}$	number of effective samples for integrity	1 [25, 26]
$N_{ES,cont}$	number of effective samples for continuity	1 [25, 26]

References

[1] S. Langel, S. Khanafseh, and B. Pervan, "Bounding Integrity Risk in the Presence of Parametric Time Correlation Uncertainty," in *Institute of Navigation International Technical Meeting 2012, ITM 2012*, vol. 2, pp. 1666–1680, 2012.

[2] S. Langel, *Bounding Estimation Integrity Risk for Linear Systems with Structured Stochastic Modeling Uncertainty.* PhD thesis, Illinois Institute of Technology, 2014.

[3] E. Gallon, M. Joerger, S. Perea, and B. Pervan, "Error Model Development for ARAIM Exploiting Satellite Motion," in *Proceedings of the ION GNSS+ 2019*, (Miami, Florida), September 2019.

[4] S. K. Jada and M. Joerger, "GMP-overbound parameter determination for measurement error time correlation modeling," *ION 2020 International Technical Meeting Proceedings*, no. 2002, pp. 189–206, 2020.

[5] S. Langel, O. García Crespillo, and M. Joerger, "A New Approach for Modeling Correlated Gaussian Errors using Frequency Domain Overbounding," *2020 IEEE/ION Position, Location and Navigation Symposium, PLANS 2020*, pp. 868–876, 2020.

[6] E. Gallon, M. Joerger, and B. Pervan, "Robust Modeling of Tropospheric Delay Dynamics for Sequential Positioning," in *IEEE/ION PLANS 2020*, (Portland, Oregon), 2020.

[7] S. K. Jada and M. Joerger, "High-Integrity Measurement Error Time Correlation Modeling Using PSD-Bounding of Experimental Data." Royal Institute of Navigation, Navigation 2021, Nov 2021.

[8] Working Group C, "EU-U.S. Cooperation on Satellite Navigation, Working Group C, ARAIM Technical Subgroup, Interim Report," tech. rep., 2012.

[9] Working Group C, "EU-US Cooperation on Satellite Navigation Working Group C, ARAIM Technical Subgroup, Milestone 2 Report," tech. rep., 2015.

[10] Working Group C, "EU-U.S. Cooperation on Satellite Navigation Working Group C, ARAIM Technical Subgroup, Milestone 3 Report," tech. rep., 2016.

[11] M. Joerger and B. Pervan, "Multi-constellation ARAIM exploiting satellite motion," *Navigation, Journal of the Institute of Navigation*, vol. 2, no. March 2019, pp. 1–19, 2020.

[12] T. Walter, K. Gunning, R. E. Phelts, and J. Blanch, "Validation of the unfaulted error bounds for ARAIM," *Proceedings of the Institute of Navigation Pacific Positioning, Navigation and Timing Meeting, Pacific PNT*, vol. 2017-May, pp. 1–19, 2017.

[13] S. Perea, M. Meurer, and B. Pervan, "Impact of sample correlation on SISRE overbound for ARAIM," *Navigation, Journal of the Institute of Navigation*, vol. 67, no. 1, pp. 197–212, 2020.

[14] S. Langel, O. García Crespillo, and M. Joerger, "Bounding Sequential Estimation Errors Due to Gauss-Markov Noise with Uncertain Time Constants," in *Proceedings of the ION GNSS+ 2019*, (Miami, Florida), September 2019.

[15] O. García Crespillo, M. Joerger, and S. Langel, "Overbounding GNSS/INS Integration with Uncertain GNSS Gauss-Markov Error Parameters," *2020 IEEE/ION Position, Location and Navigation Symposium, PLANS 2020*, pp. 481–489, 2020.

[16] O. García Crespillo, M. Joerger, and S. Langel, "Tight Bounds for Uncertain Time-Correlated Errors with Gauss-Markov Structure," 2020.

[17] S. Langel, O. García Crespillo, and M. Joerger, "Overbounding Sequential Estimation Errors Due to Non-Gaussian Correlated Noise," *Proceedings of the 33rd International Technical Meeting of the Satellite Division of The Institute of Navigation (ION GNSS+ 2020)*, pp. 1054–1067, 2020.

[18] E. Gallon, M. Joerger, and B. Pervan, "Frequency-Domain Modeling of Orbit and Clock Errors for Sequential Positioning," in *ION GNSS+ 2020*, (St. Louis, Missouri), 2020.

[19] S. Langel, O. García Crespillo, and M. Joerger, "Overbounding the effect of uncertain Gauss-Markov noise in Kalman filtering," *Navigation, Journal of the Institute of Navigation*, vol. 68, no. 2, pp. 259–276, 2021.

[20] E. Gallon, M. Joerger, and B. Pervan, "Robust Modeling of GNSS Tropospheric Delay Dynamics," *IEEE Transactions on Aerospace and Electronic Systems*, 2021.

[21] E. Gallon, M. Joerger, and B. Pervan, "Robust Modeling of GNSS Orbit and Clock Error Dynamics," 2021.

[22] B. Pervan, S. Khanafseh, and J. Patel, "Test Statistic Auto- and Cross-correlation Effects on Monitor False Alert and Missed Detection Probabilities," in *Proceedings of the 2017 International Technical Meeting of The Institute of Navigation*, (Monterey, California), pp. 562–590, January 2017.

[23] J. Haase, M. Ge, H. Vedel, and E. Calais, "Accuracy and Variability of GPS Tropospheric Delay Measurements of Water Vapor in the Western Mediterranean," *Journal of Applied Meteorology)*, vol. 42, pp. 1547–1568, November 2003.

[24] C. Chatfield, *The analysis of time series: An introduction*, ch. Spectral Analysis. Boca Raton, FL, USA: CRC Press, 6 ed., 2003.

[25] C. Milner, B. Pervan, J. Blanch, and M. Joerger, "Evaluating Integrity and Continuity Over Time in Advanced RAIM," *2020 IEEE/ION Position, Location and Navigation Symposium, PLANS 2020*, pp. 502–514, 2020.

[26] Working Group C, "WG-C Advanced RAIM Technical Subgroup Reference Airborne Algorithm Description Document," tech. rep., May 2019.

[27] D. Racelis and M. Joerger, "Impact of Cascading Faults on Mega-Constellation-Augmented GNSS PPP Integrity," *Proceedings of the 33rd International Technical Meeting of the Satellite Division of The Institute of Navigation (ION GNSS+ 2020)*, pp. 3055–3070, 2020.

[28] T. Walter, J. Blanch, and P. Enge, "Evaluation of Signal in Space Error Bounds to Support Aviation Integrity," *Navigation, Journal of the Institute of Navigation)*, vol. 57, no. 2, pp. 101–113, Summer 2010.

[29] T. Walter and J. Blanch, "KEYNOTE - Characterization of GNSS Clock and Ephemeris Errors to Support ARAIM," in *Proceedings of the ION 2015 Pacific PNT Meeting*, (Honolulu, Hawaii), pp. 920–931, April 2015.

[30] T. Walter, K. Gunning, R. Eric Phelts, and J. Blanch, "Validation of the Unfaulted Error Bounds for ARAIM," *Navigation, Journal of The Institute of Navigation*, vol. 65, no. 1, pp. 117–133, 2018.

[31] Radio Technical Commission for Aeronautics (RTCA) Special Committee 159, "Minimum Operational Performance Standards for Global Positioning System/Wide Area Augmentation System Airborne Equipment," 2006.

[32] Radio Technical Commission for Aeronautics (RTCA) Special Committee 159, "Minimum Operational Performance Standards for Global Positioning System/Wide Area Augmentation System Airborne Equipment," 2009.

[33] D. Lawrence, *Aircraft Landing Using GPS: Development and Evaluation of a Real Time System for Kinematic Position using the Global Positioning System*. PhD thesis, Stanford University, 1996.

[34] D. Racelis, M. Joerger, and B. Pervan, "Fault-Free Integrity Analysis of Mega-Constellation-Augmented GNSS," in *32nd International Technical Meeting of the Satellite Division of the Institute of Navigation, ION GNSS+ 2019*, pp. 465–484, 2019.

[35] U.S. Department of Defense, *Global Positioning System Standard Positioning Service Performance Standard (GPS SPS PS)*. 5 ed., April 2020.